Aggregation state determines the localization and function of M1– and M23–aquaporin-4 in astrocytes

Alex J. Smith, Byung-Ju Jin, Julien Ratelade, and Alan S. Verkman

Departments of Medicine and Physiology, University of California, San Francisco, San Francisco, CA 94143

The astrocyte water channel aquaporin-4 (AQP4) is expressed as heterotetramers of M1 and M23 isoforms in which the presence of M23–AQP4 promotes formation of large macromolecular aggregates termed orthogonal arrays. Here, we demonstrate that the AQP4 aggregation state determines its subcellular localization and cellular functions. Individually expressed M1–AQP4 was freely mobile in the plasma membrane and could diffuse into rapidly extending lamellipodial regions to support cell migration. In contrast, M23–AQP4 formed large arrays that did not diffuse rapidly enough to enter lamellipodia and instead stably bound adhesion complexes and polarized to astrocyte end-feet in vivo. Co-expressed M1– and M23–AQP4 formed aggregates of variable size that segregated due to diffusional sieving of small, mobile M1–AQP4-enriched arrays into lamellipodia and preferential interaction of large, M23–AQP4-enriched arrays with the extracellular matrix. Our results therefore demonstrate an aggregation state–dependent mechanism for segregation of plasma membrane protein complexes that confers specific functional roles to M1– and M23–AQP4.

Introduction

Aquaporin-4 (AQP4) water channels are expressed in astrocytes throughout the central nervous system where they facilitate water transport across the blood–brain barrier, clearance of extracellular K^+ after neuronal excitation, and cell migration in response to injury (Papadopoulos and Verkman, 2013). AQP4-deficient mice show reduced cytotoxic brain swelling but increased vasogenic brain swelling (Manley et al., 2000; Papadopoulos et al., 2004), abnormal patterns of seizure activity and cortical spreading depression (Padmawar et al., 2005; Binder et al., 2006), and impaired astrocyte migration and glial scar formation (Saadoun et al., 2005b; Auguste et al., 2007). AQP4 is highly enriched at astrocyte end-feet (Nielsen et al., 1997), but can also polarize to the leading edge of migrating astrocytes where it facilitates lamellipodial extension and increases cell migration (Saadoun et al., 2005b).

AQP4 is expressed as two principal isoforms; a long isoform with translation initiation at Met-1 (M1–AQP4) and a short isoform with translation initiation at Met-23 (M23–AQP4; Jung et al., 1994; Yang et al., 1995; Lu et al., 1996). M1–AQP4 and M23–AQP4 form heterotetramers (Neely et al., 1999) that further assemble into crystal-like supramolecular aggregates called orthogonal arrays (Landis and Reese, 1974; Yang et al., 1996). Each isoform has similar water permeability but different aggregation properties; intermolecular interactions between M23–AQP4 molecules on adjacent tetramers involving hydrophobic residues downstream from Met-23 promote array formation (Crane and Verkman, 2009), but palmitoylation-dependent anchoring of the N terminus of M1–AQP4 to the membrane blocks these interactions and homotetramers of M1–AQP4 do not form aggregates (Suzuki et al., 2008). A model based on random M1–M23 association in heterotetramers and intermolecular M23–M23 interactions predicts the size distribution of orthogonal arrays generated at different ratios of M1/M23 expression (Jin et al., 2011), and super-resolution imaging has demonstrated that orthogonal arrays of particles (OAPs) consisting of an M23-enriched core surrounded by an M1-enriched periphery are formed in cells expressing both isoforms (Rossi et al., 2012a).

The functional significance of the two AQP4 isoforms and their distinctive supramolecular aggregation pattern has been

Correspondence to Alan S. Verkman: alan.verkman@ucsf.edu

Abbreviations used in this paper: AQP4, aquaporin-4; *d*STORM, direct stochastic optical reconstruction microscopy; GFAP, glial fibrillary acidic protein; NMO, neuromyelitis optica; OAPs, orthogonal arrays of particles.

The Rockefeller University Press $30.00
J. Cell Biol. Vol. 204 No. 4 559–573
www.jcb.org/cgi/doi/10.1083/jcb.201308118

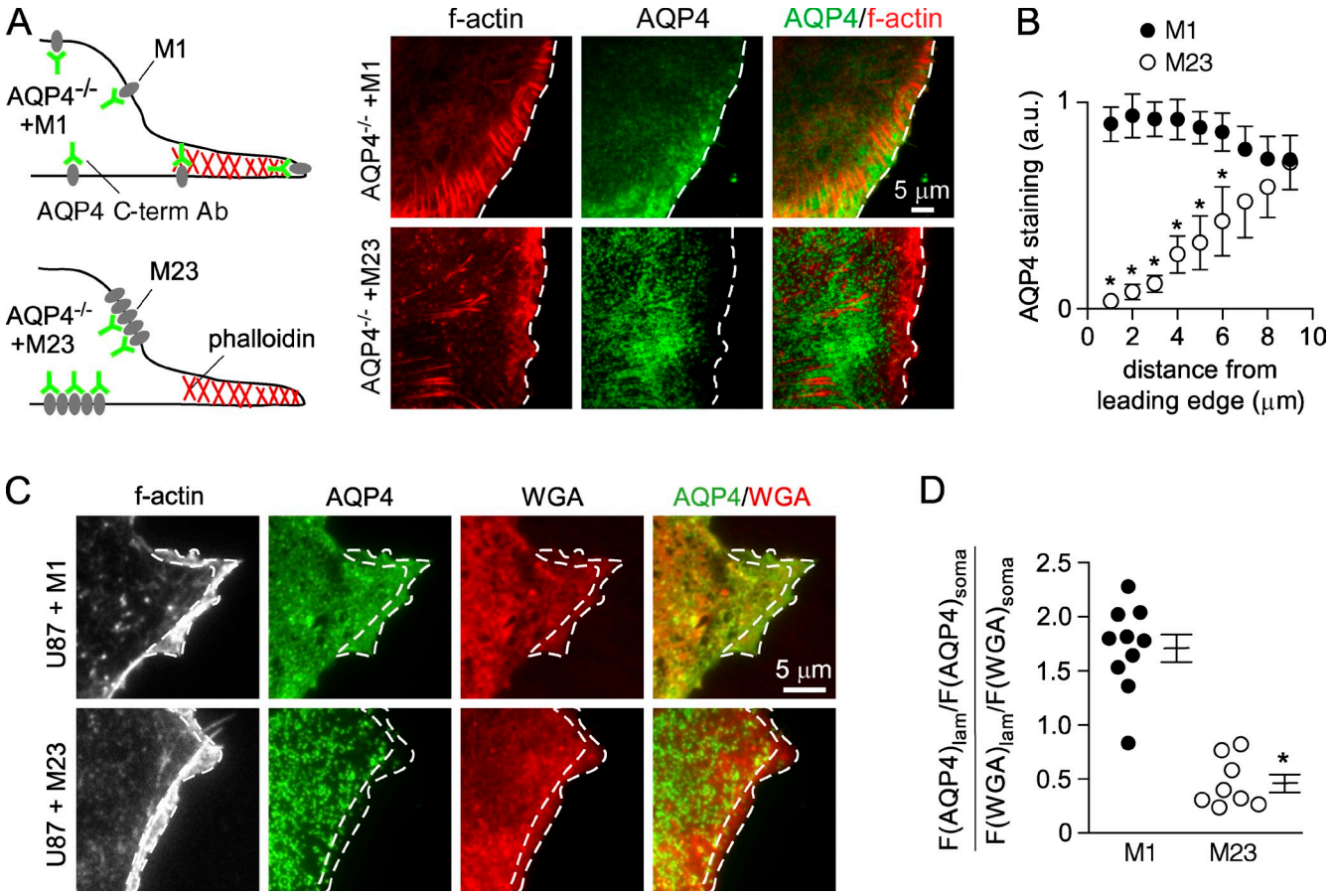

Figure 1. **M1–AQP4, but not M23–AQP4, localizes to the leading edge of migrating astrocytes and glioma cells.** (A) Schematic showing predicted distribution of M1– or M23–AQP4 and F-actin labeling in migrating cells and TIRF images showing F-actin and AQP4 distribution in M1- and M23-transfected AQP4$^{-/-}$ astrocytes during migration into a scratch wound. White dashed line demarcates the cell leading edge. (B) AQP4 staining intensity as a function of distance from the leading edge for cells labeled as in A (mean ± SE, 10 cells; *, $P < 0.05$ between M1 and M23 by *t* test at the indicated distance). (C) F-actin, AQP4, and wheat germ agglutinin (WGA) labeling in randomly migrating U87-MG cells transfected with M1– or M23–AQP4. (D) Ratio of mean AQP4 staining intensity in F-actin–rich lamellipodial (outlined) and somatic (rest of image) regions normalized to the ratio of WGA staining intensity in the same regions (mean ± SE, 10 cells; *, $P < 0.001$).

unclear. Here, we demonstrate that macromolecular aggregation state determines the subcellular localization of M1– and M23–AQP4 and this translates to distinct functions in cell migration and polarization.

Results

Different cellular localization of M1- and M23-AQP4 expressed individually in migrating astrocytes and glioma cells

Wild-type astrocytes express both M1– and M23–AQP4 and show polarization of AQP4 toward the leading edge when migrating into a scratch wound (Saadoun et al., 2005b). We transfected cortical astrocyte cultures, generated from AQP4$^{-/-}$ mice, with adenovirus encoding M1– or M23–AQP4 (Li et al., 2011) and measured recruitment of each isoform to the leading edge of cells migrating into a scratch wound. M1–AQP4 showed diffuse staining throughout the cell membrane with some enrichment in lamellipodia, but M23–AQP4 aggregates were excluded from leading-edge areas (Fig. 1, A and B).

AQP4 expression is strongly up-regulated in high grade gliomas (Saadoun et al., 2002), where it may contribute to tumor cell motility and invasiveness, but expression is rapidly lost after passage in culture (McCoy and Sontheimer, 2007). The human glioblastoma-derived cell line U87-MG forms transient lamellipodial-like protrusions when migrating on fibronectin at low density (Caspani et al., 2006). We investigated recruitment of transfected M1– or M23–AQP4 into these structures. M1–AQP4 was enriched in actin-rich protrusions relative to wheat germ agglutinin (used as a plasma membrane marker), whereas M23–AQP4 was largely excluded (Fig. 1, C and D), as found in the astrocyte cultures. These results demonstrate a specific requirement for the M1- isoform during recruitment of AQP4 to the leading edge of migrating cells in culture.

Leading-edge translocation of AQP4 was further studied in live cells using fluorescent protein fusions and TIRF microscopy. U87-MG cells were transfected with fluorescent AQP4 chimeras containing GFP at the C terminus of M1– and M23–AQP4, which do not interfere with AQP4 surface transport or OAP assembly (Tajima et al., 2010). Lamellipodial extensions were visualized by cotransfection with mCherry fused to the

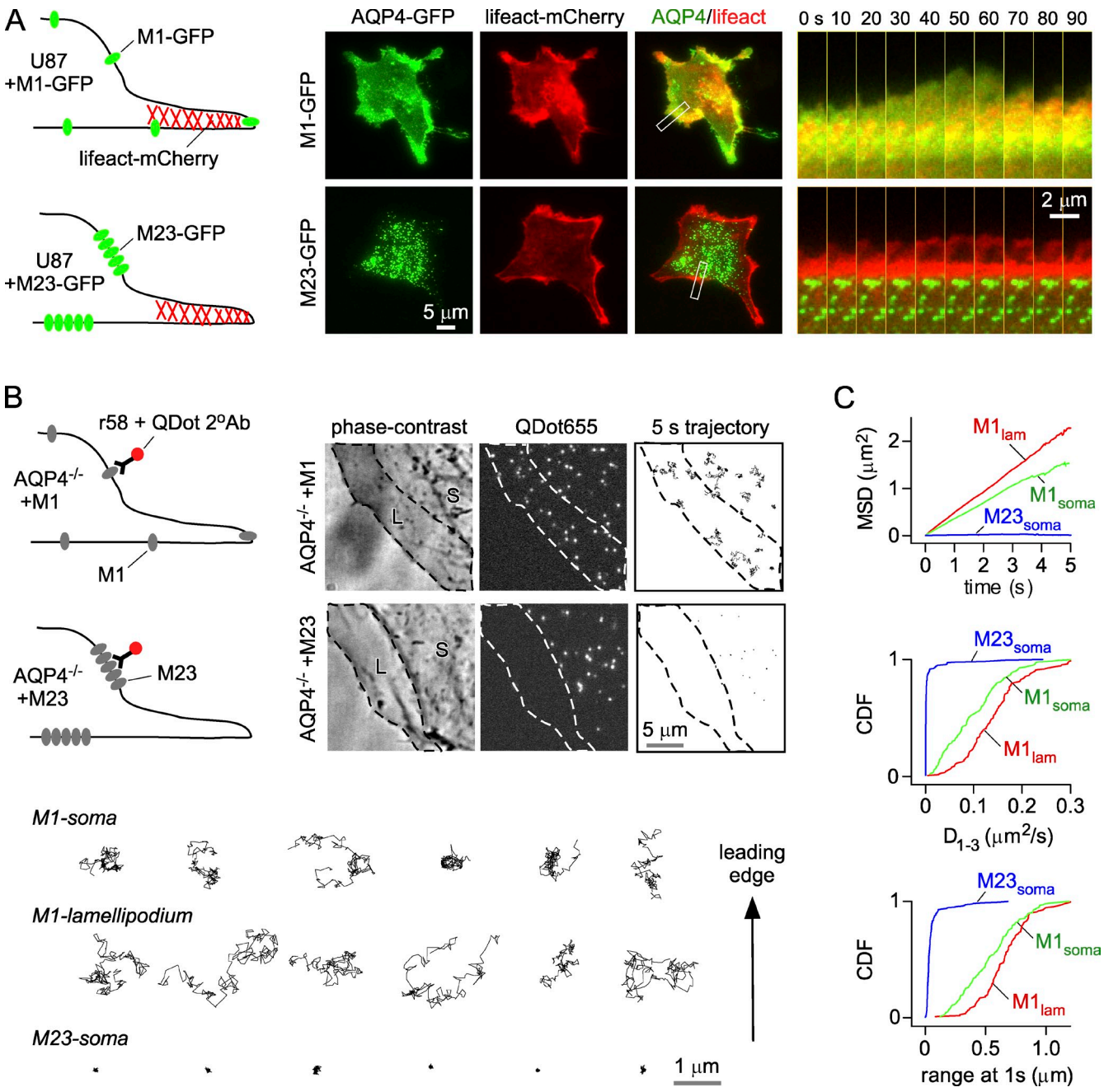

Figure 2. **Dynamics of M1–AQP4 translocation to the leading edge in live, migrating astrocytes and glioma cells.** (A) AQP4-GFP dynamics in randomly migrating U87-MG cells cotransfected with M1– or M23–AQP4–GFP and mCherry-LifeAct (to visualize F-actin–enriched lamellipodial protrusions). Center panels show single full frames and right panels show images of a sub-region (white rectangular box) at 10-s intervals during a cycle of lamellipodial protrusion and retraction. (B) Quantum dot, single-particle tracking in lamellipodial and somatic regions of AQP4$^{-/-}$ astrocytes transfected with M1– or M23–AQP4 and labeled with mAb r58 (binds an extracellular epitope on AQP4) and QDot-conjugated secondary Ab. Lamellipodial regions were identified from phase-contrast images taken immediately before QDot tracking and overlayed on reconstructed trajectories, allowing their assignment to lamellipodial (L) or somatic (S) analysis groups (top panels). Bottom panels show representative reconstructed trajectories over 5 s of M1–AQP4 in somatic or lamellipodial regions or of M23–AQP4 in somatic regions oriented so the leading edge is in the direction of the arrow. (C) Pooled analysis of 100–150 separate AQP4 trajectories in somatic and lamellipodial regions of 10–12 astrocytes transfected with either M1– or M23–AQP4, shown as the average mean-squared displacement vs. time (top) and the cumulative distribution function of short-range (0–100 ms) diffusion coefficient (middle) and range at 1 s (bottom).

actin-binding protein LifeAct (Riedl et al., 2008). Fig. 2 A and Videos 1 and 2 demonstrate rapid access of M1–AQP4–GFP in extending lamellipodia, whereas M23–AQP4–GFP, seen as distinct puncta representing orthogonal arrays, was excluded.

We also characterized the movement of single AQP4 molecules into the lamellipodia of migrating astrocytes by quantum dot single-particle tracking using a monoclonal antibody that recognizes an extracellular epitope common to M1– and M23–AQP4 (mAb r58; Crane et al., 2009). In M1–AQP4-transfected cells, quantum dot labeling was seen in both lamellipodial and nonlamellipodial regions, whereas in M23–AQP4-transfected cells labeling was largely confined to nonlamellipodial regions

of the plasma membrane (Fig. 2 B, top). Reconstructed single-particle trajectories showed apparent Brownian movement of M1–AQP4 in both lamellipodial and adjacent somatic regions of the plasma membrane, whereas M23–AQP4 was largely immobile over the 10-s recording time (Fig. 2 B, bottom). The mean-squared displacement vs. time relationship was linear for M1–AQP4 in both areas, without evidence for convective movement of M1–AQP4 toward the leading edge (Fig. 2, B and C). Cumulative distribution plots of short-range diffusion coefficient ($D_{1–3}$) and range at 1 s showed mildly increased diffusion of M1–AQP4 in lamellipodial vs. somatic regions, which appeared to result from the absence of a low-mobility population of M1–AQP4 in lamellipodia (Fig. 2 C, all distributions are significantly different [$P < 0.001$] by Kolmogorov-Smirnoff test). As expected, M23–AQP4 was nearly immobile in somatic regions (Fig. 2, B and C). These results demonstrate that diffusional mobility determines entry of AQP4 into the lamellipodial compartment and explain the absence of relatively immobile M23–AQP4 aggregates from the leading edge.

Size, composition, and mobility-dependent sieving of orthogonal arrays containing both M1- and M23-AQP4

The results in Figs. 1 and 2 show clear-cut differential localization of separately expressed M1– versus M23–AQP4. When coexpressed in the same cell the two isoforms form heterotetramers (Neely et al., 1999), which further assemble into orthogonal arrays whose size is determined by the number of M23–AQP4 subunits available to participate in intra-tetramer interactions (Furman et al., 2003; Jin et al., 2011; Rossi et al., 2012b). Diffusional mobility of orthogonal arrays containing both M1– and M23–AQP4 is highly dependent on the size, and consequently the M1/M23 ratio, of each individual aggregate. Heterogeneity in the population of orthogonal arrays is demonstrated by the observation that the range moved in 1 s by individual AQP4 particles varies by more than two orders of magnitude in cells transfected with both M1– and M23–AQP4 (Crane et al., 2009). These observations led us to hypothesize that segregation of M1– and M23–AQP4 might occur in cells expressing both isoforms due to "diffusional sieving," where relatively small and mobile aggregates enriched in M1–AQP4 diffuse into transiently formed lamellipodia, and larger, M23 enriched aggregates do not.

To test this we cotransfected U87-MG cells with M1–AQP4–GFP and M23–AQP4–mCherry and measured the ratio of GFP to mCherry fluorescence in actin-rich lamellipodial and nonlamellipodial (somatic) regions. Fig. 3 (A and B) and Video 3 show partial segregation of M1– and M23–AQP4 under these conditions; the ratio of M1/M23 fluorescence intensity was on average 45% higher in actin-rich lamellipodial areas than in nonlamellipodial areas, demonstrating preferential enrichment of M1-GFP at the cell periphery and in lamellipodia even under conditions where M1– and M23–AQP4 form heterotetramers. To detect segregation of native (nontagged) M1– and M23–AQP4, we used two monoclonal anti-AQP4 antibodies derived from neuromyelitis optica (NMO) patients, one of which (r93) recognizes AQP4 only in orthogonal arrays and another (r58) that recognizes all AQP4 (Crane et al., 2009). Fig. 3 C shows that, as expected, mAb r93 binds U87-MG cells expressing M23–AQP4 but not M1–AQP4, whereas mAb r58 binds to cells expressing either M1– or M23–AQP4. In cells expressing both M1– and M23–AQP4 the ratio of r93 staining to total AQP4 staining in lamellipodia was significantly lower than the ratio of r93 to total AQP4 in the soma, whereas no significant difference in the ratio of r58 to AQP4 staining was observed between the two compartments (Fig. 3, D and E). This result provides further evidence that large arrays are selectively excluded from the lamellipodial plasma membrane.

Direct stochastic optical reconstruction microscopy (*d*STORM) can be used to estimate AQP4 array size in cells transfected with M1– and M23–AQP4 at different ratios (Rossi et al., 2012b). We performed experiments to determine if this method could be used to measure differences in AQP4 array size in lamellipodial and somatic plasma membrane. In TIRF images of U87-MG cells coexpressing M1– and M23–AQP4 at a 1:3 ratio (as found in native astrocytes in vivo), AQP4 arrays in lamellipodia had generally lower fluorescence than those in soma, indicating a reduced number of AQP4 molecules per spot in lamellipodia and hence reduced array size (Fig. 4 A, left). *d*STORM imaging of the same cells, under conditions giving ∼20 nm spatial resolution, showed relatively larger aggregates in soma than lamellipodia (Fig. 4 A, right). In addition, we measured array sizes in wild-type astrocytes that natively express both M1– and M23–AQP4 at a ratio of ∼1:1 in vitro. Fig. 4 B shows the distribution of size for the somatic and lamellipodial AQP4 populations derived from the cells shown in Fig. 4 A. The median aggregation state of AQP4 (aggregate size at which 50% of AQP4 is in smaller/larger aggregates) in U87-MG cells (transfected at 1M1:3M23) was 7,560 ± 640 nm^2 in lamellipodia and 13,300 ± 964 nm^2 in soma ($n = 6$ cells, $P < 0.01$ by paired t test); in cultured wild-type astrocytes (1M1:1M23) it was 4,250 ± 320 nm^2 in lamellipodia and 5,630 ± 315 nm^2 in soma ($n = 4$ cells, $P < 0.05$ by paired t test).

A final prediction of diffusional sieving is that AQP4 aggregates with higher mobility are relatively enriched in lamellipodial plasma membrane compared with somatic plasma membrane of cells coexpressing M1– and M23–AQP4. To test this prediction we performed quantum dot single-particle tracking, as done in Fig. 2 B, in wild-type astrocytes. Fig. 4 C shows representative trajectories in lamellipodia and soma. Mean-squared displacement analysis and cumulative probability plots indicate more rapid quantum dot diffusion in lamellipodia than soma and the absence of low mobility aggregates from the lamellipodial membrane (Fig. 4 D; distribution of range and diffusion coefficients differ with $P < 0.001$ by Kolmogorov-Smirnoff test), thereby confirming that small, high mobility aggregates are present at higher density in the lamellipodial plasma membrane.

Mathematical modeling supports a diffusional sieving mechanism

In prior work we computed the size and composition of individual AQP4 arrays generated at different ratios of M1– and M23–AQP4 (Jin et al., 2011). Here, we used the orthogonal array size

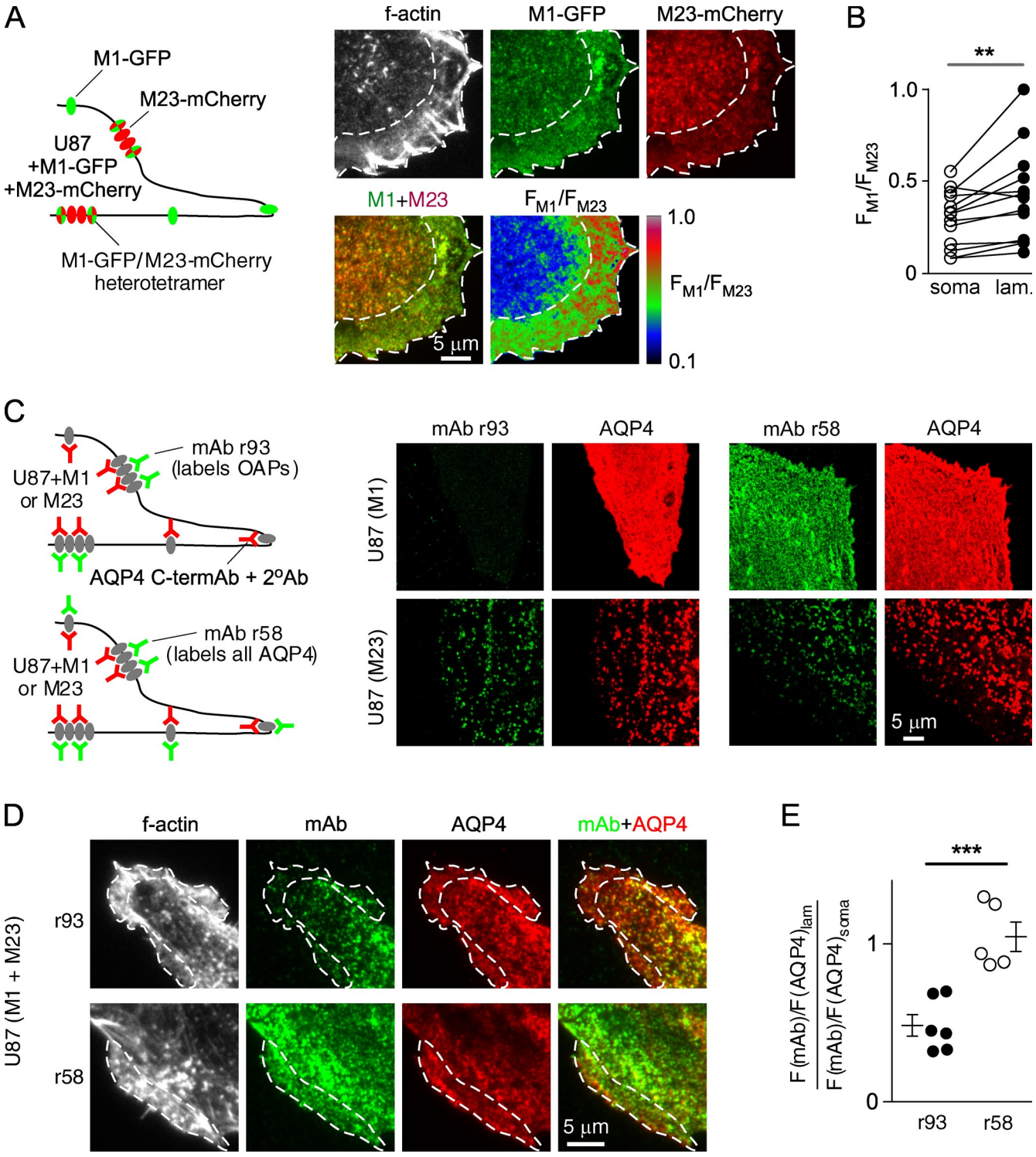

Figure 3. **Partial segregation of M1– and M23–AQP4 in lamellipodial and somatic regions of cells expressing both isoforms.** (A) Schematic showing predicted distribution of M1–AQP4–GFP and M23–AQP4–mCherry in migrating cells and TIRF images of U87-MG cells transfected with both isoforms then fixed and stained with phalloidin showing localization of M1– and M23–AQP4 in relation to an actin enriched membrane extension. (B) Ratio of M1/M23 fluorescence intensity in somatic and lamellipodial regions of individual U87-MG cells. **, $P < 0.01$ by paired *t* test, $n = 8$. (C) Schematic showing predicted distribution of labeling with monoclonal antibodies (mAbs) specific for only orthogonal arrays (r93) or for all AQP4 (r58) in migrating cells expressing both M1– and M23–AQP4 and confocal images demonstrating that mAb r93 does not bind to cells transfected with only M1–AQP4, whereas r58 binds to cells transfected with M1– or M23–AQP4. (D) TIRF images showing labeling of F-actin, total AQP4, and r93 or r58 mAbs in migrating U87-MG cells transfected with M1– and M23–AQP4. (E) Quantification of the relative amount of AQP4 stained with each mAb in lamellipodial compared with somatic regions of cells stained with r58 ($n = 5$) or r93 ($n = 6$). ***, $P < 0.001$ between r58 and r93 groups by *t* test.

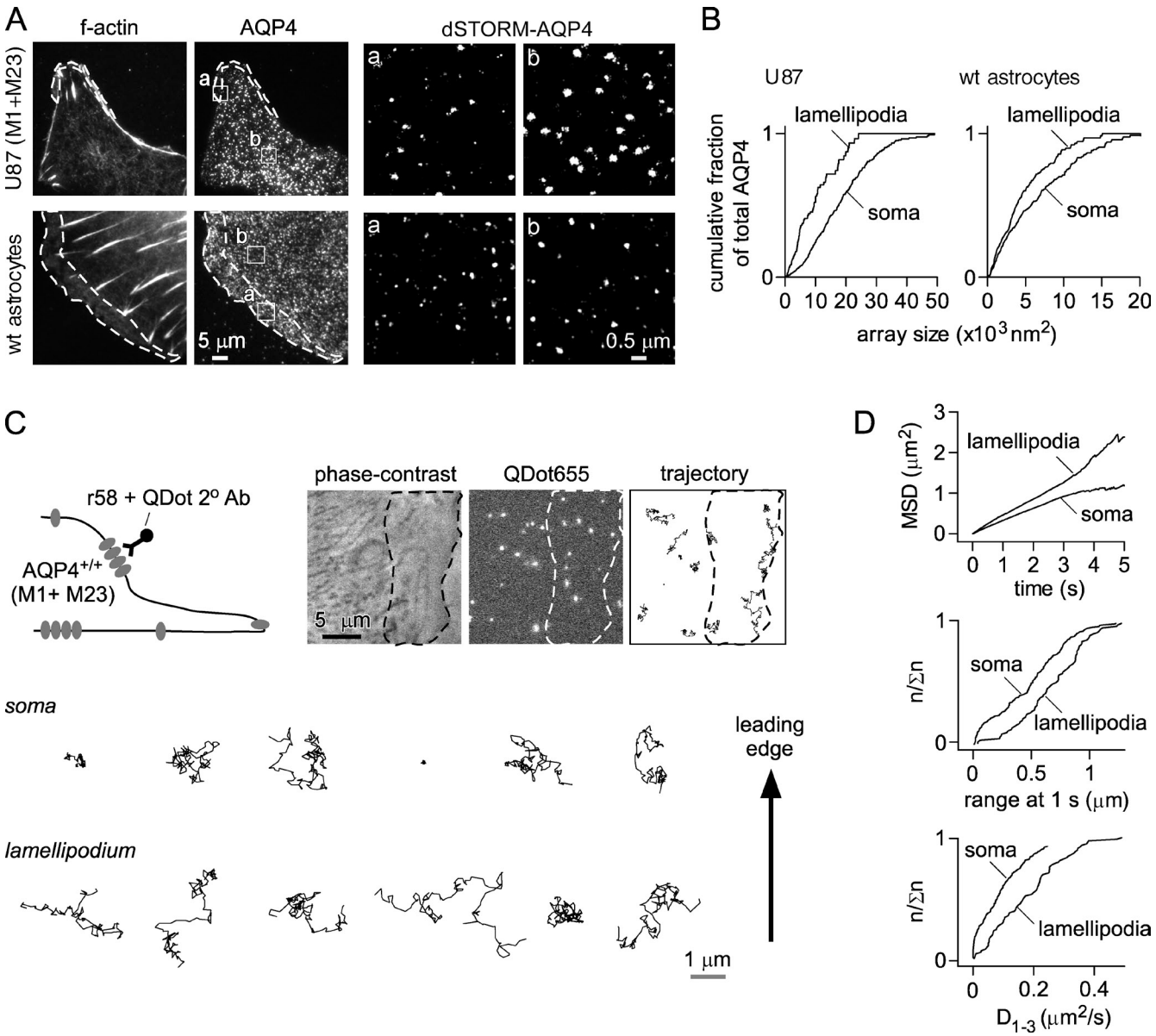

Figure 4. **Orthogonal arrays have different size and diffusional mobility in somatic and lamellipodial plasma membrane of cells expressing both M1– and M23–AQP4.** (A) Left panels show TIRF images of AQP4 and F-actin in U87-MG cells cotransfected with M1– and M23–AQP4, and in wild-type astrocyte cultures (that express both isoforms). Right panels show reconstructed *d*STORM images of AQP4 from the indicated areas (white boxes). (B) Cumulative distribution of AQP4 by array size in lamellipodial and somatic regions from cells shown in A. (C) Qdot single-particle tracking of AQP4 in lamellipodial and somatic regions of wild-type astrocytes (top panels) with representative trajectories from lamellipodial and somatic areas shown in bottom panels. (D) Pooled analysis of 216 somatic and 80 lamellipodial trajectories from 10 cells shown as the average mean-squared displacement vs. time (top) and cumulative probability plots of range at 1 s (middle) and short-range (0–100 ms) diffusion coefficient (bottom).

and composition predicted by this model to determine if a size-dependent diffusional mechanism could explain the experimentally observed segregation of coexpressed M1– and M23–AQP4. As the diffusion of large orthogonal arrays is highly confined (Crane et al., 2008), the relationship between aggregate size and diffusion coefficient deviates substantially from that predicted by a consideration of cross-sectional radius alone. We empirically fitted an exponential function to the experimentally measured average AQP4 diffusion coefficient and array size in cells with defined M1/M23 expression ratios (Fig. 5 A; Crane et al., 2009; Rossi et al., 2012b). Simulated AQP4 arrays, with size, diffusion coefficient, and composition computed from a specified M1/M23 expression ratio were distributed randomly throughout the cell plasma membrane (Fig. 5 B). A single lamellipodial extension with typical linear velocity of 0.5 μm/min over 10 min was created at the leading edge of the cell, and AQP4 particles were allowed to diffuse freely into the newly created space.

Videos 4 and 5 show simulations for M1/M23 ratios of 1:1 and 1:3. Fig. 5 C shows the distribution of AQP4 particle sizes (encoded by dot size) and M1/M23 composition (encoded by color) in lamellipodial and somatic plasma membrane. AQP4 diffusion into lamellipodial extensions depended strongly on M1/M23 content, with marked diffusion of M1–AQP4 into

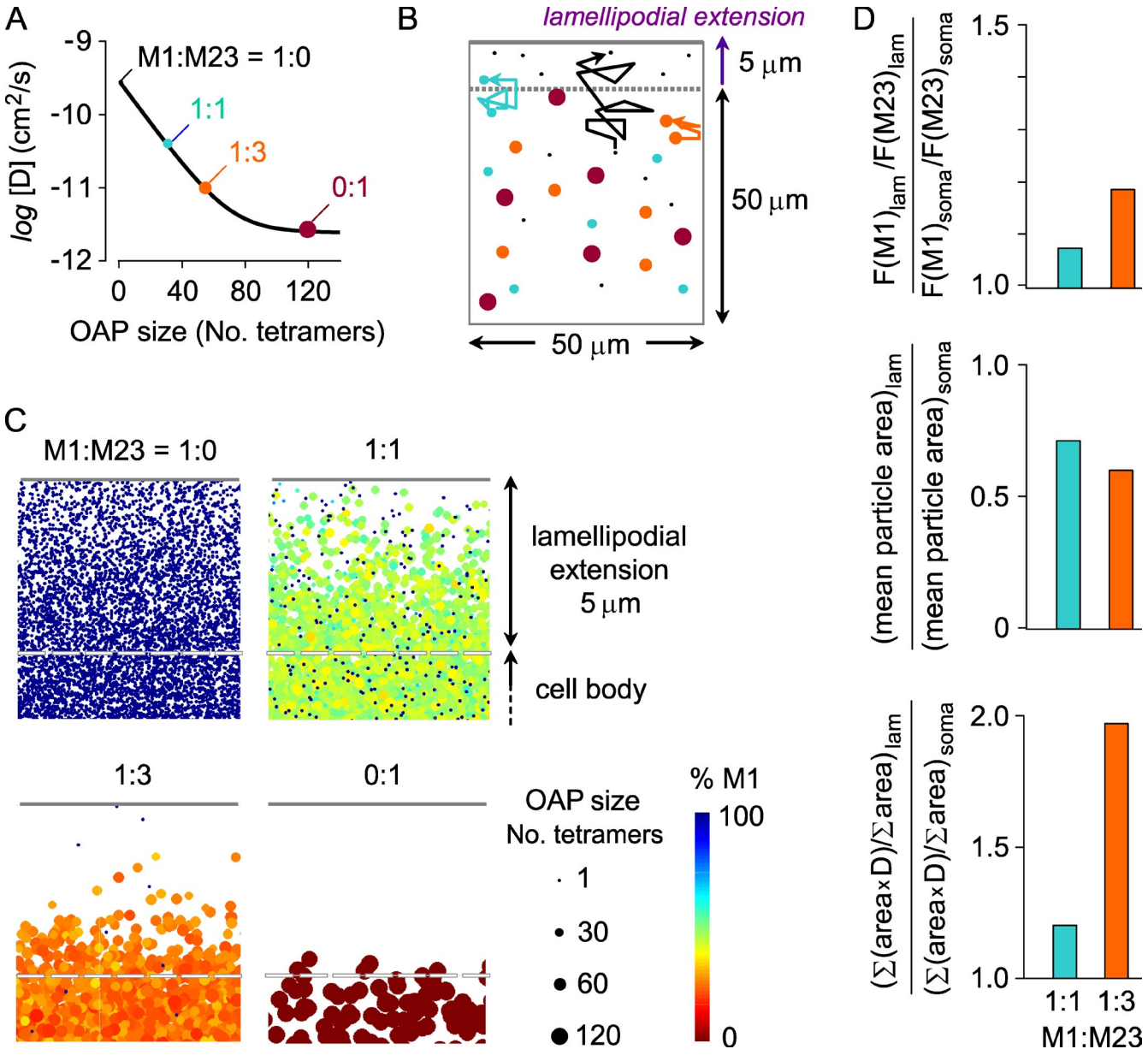

Figure 5. **Modeling of AQP4 diffusion in the plasma membrane of extending lamellipodia predicts size- and composition-dependent sieving of orthogonal arrays.** (A) Dependence of AQP4 diffusion coefficient, D, on array size (number of tetramers/array), deduced from single-particle tracking data (Crane et al., 2009) and *d*STORM imaging (Rossi et al., 2012b). (B) Schematic showing two-dimensional diffusion of AQP4 particles into an extending lamellipodium of length 5 µm, with 50 µm × 50 µm cell body. (C) Computations showing the distribution of AQP4 particles just after a lamellipodia extension, for indicated M1/M23 ratios of 1:0, 1:1, 1:3, and 0:1. Filled circles encode particle sizes, and color encodes percentage of M1–AQP4 in each particle. (D) Distribution of AQP4 isoforms, size, and diffusion computed just after a lamellipodial extension for M1/M23 of 1:1 and 1:3. Computations show relative M1–AQP4 enrichment in lamellipodia (top), with reduced AQP4 array size (middle), and increased AQP4 diffusion (bottom).

lamellipodia but little diffusion of M23–AQP4, as found experimentally. Fig. 5 D summarizes the relative lamellipodial enrichment of M1– versus M23–AQP4 (top), particle size (middle), and particle diffusion (bottom) in simulations on cells coexpressing M1– and M23–AQP4, which are in close agreement with experimental findings from cells in Figs. 3 and 4. These computations provide a quantitative basis for the hypothesis that a simple diffusional sieving mechanism can account for the experimentally observed segregation of coexpressed AQP4 isoforms in lamellipodial and somatic plasma membrane. Interactions of large orthogonal arrays with adhesion complexes (see next section) may further retard diffusion of M23–AQP4 on the basal surface of cultured cells in vivo, also contributing to segregation of large and small arrays.

Distinct functions of M1- and M23-AQP4 in astrocyte migration and polarization

We previously reported impaired migration of astrocytes from AQP4 knockout mice both in vitro (Saadoun et al., 2005b) and in vivo (Auguste et al., 2007). We postulated that access of AQP4 to the leading edge of migrating cells, and hence expression of M1–AQP4, would be required for AQP4-dependent cell

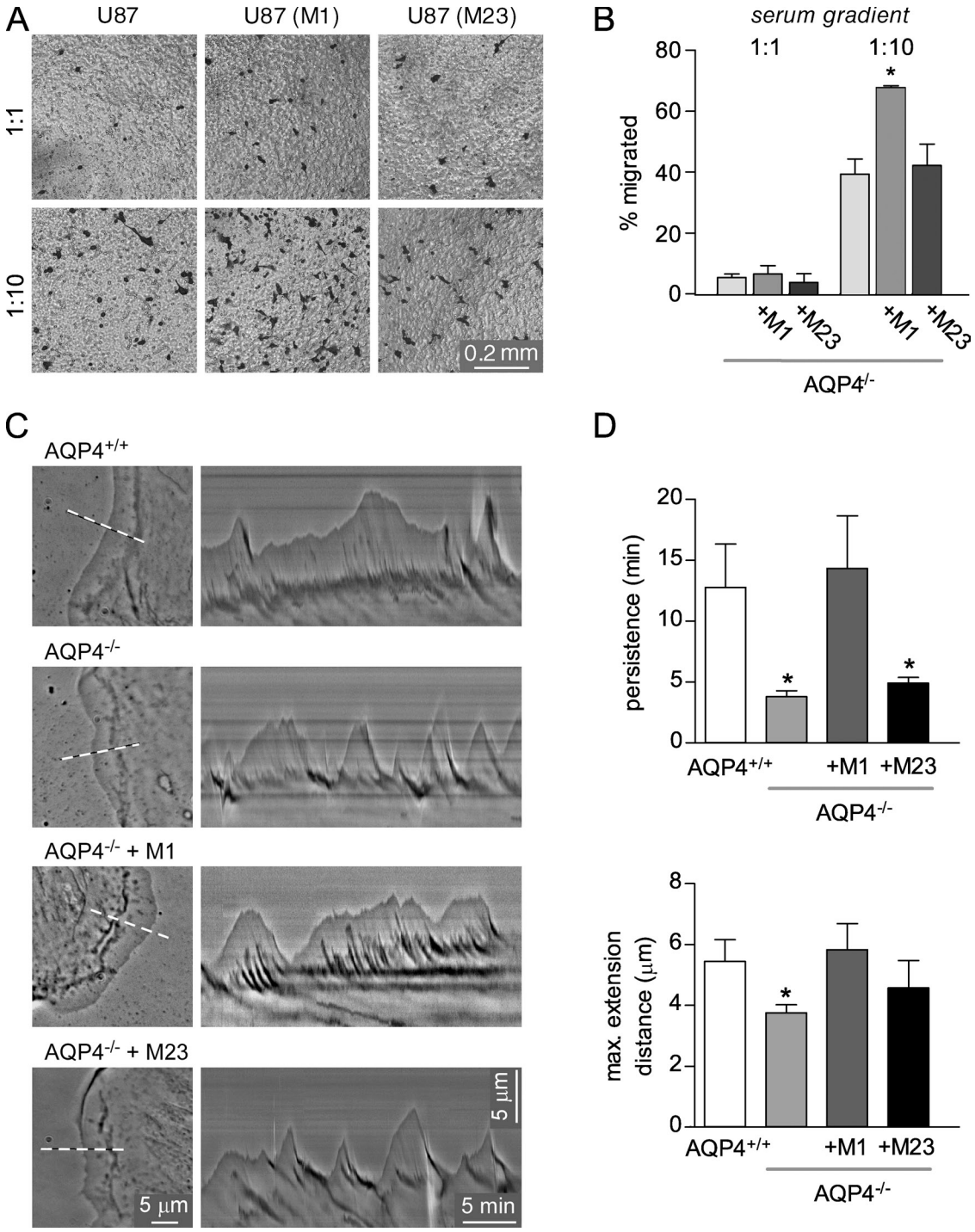

Figure 6. **M1–AQP4, but not M23–AQP4, enhances cell migration and increases lamellipodial stability.** (A) Phase-contrast images of Coomassie-stained U87-MG cells (nontransfected or stably expressing M1– or M23–AQP4) after migration through 8-µm pore Transwells in the presence of a 1–1% or 1–10% FBS gradient. (B) Percentage of cells that migrated across Transwells under each condition. Bars indicate mean ± SE, $n = 3$ each; *, $P < 0.05$ by *t* test. (C) Phase-contrast images (left) and kymographs (right) of astrocytes of the indicated genotype migrating into a scratch wound generated by re-slicing 30-min video sequences along the indicated lines. (D) Mean lamellipodial extension duration and distance in kymographs from 5–8 cells for each condition. Bars indicate mean ± SE; *, $P < 0.05$ vs. $AQP4^{+/+}$ by *t* test.

migration. First, migration of U87-MG cells stably transfected with either M1– or M23–AQP4 was measured across Transwell filters. In the presence of a serum gradient (1–10% FBS), M1–AQP4-expressing cells migrated more rapidly than the parental (AQP4 deficient) cell line, whereas M23–AQP4 expression did not increase cell migration (Fig. 6, A and B).

Defective cell migration is often associated with altered lamellipodial stability (Petrie et al., 2009). To determine if leading-edge AQP4 regulates lamellipodial dynamics we performed time-lapse phase-contrast microscopy in migrating $AQP4^{+/+}$ and $AQP4^{-/-}$ astrocytes, and in $AQP4^{-/-}$ astrocytes virally infected with M1– or M23–AQP4. As shown in representative kymograms

in Fig. 6 C (and in Video 6), lamellipodial stability was reduced in cells lacking AQP4. Significantly reduced lamellipodial duration (average time between lamellipodial retractions) and extension length (average maximum extension) were found in AQP4$^{-/-}$ astrocytes (Fig. 6 D). These defects in lamellipodial stability were rescued by transfection with M1–AQP4 but not M23–AQP4. Therefore, M1–AQP4 but not M23–AQP4 facilitates cell migration and lamellipodial stability, demonstrating that leading-edge translocation and high surface mobility of AQP4 are required in migrating cells.

AQP4 is highly enriched at astrocyte end-feet, where it is anchored to the basement membrane by interactions with adhesion complexes (Neely et al., 2001). We postulated that M1– and M23–AQP4 may play different roles in this process, reasoning that clustered AQP4 may form more stable interactions with adhesion complexes than individual AQP4 tetramers. Live-cell detergent extraction can be used to assess localization of specific molecules to adhesion sites (Boiko et al., 2007; Zhang et al., 2012), and we applied this method in U87-MG cells expressing M1– or M23–AQP4 and plated on fibronectin-coated coverglasses. Remarkably, more M23–AQP4 remained bound to the substrate after detergent treatment in M23–AQP4- than in M1–AQP4-transfected cells (Fig. 7, A and B), despite complete cell disruption as confirmed by loss of F-actin staining. We also measured the M1/M23 ratio in adherent AQP4 complexes in cells cotransfected with M1–AQP4–GFP and M23–AQP4–mCherry. Detergent-resistant arrays contained both M1– and M23–AQP4, but were enriched in M23–AQP4 (Fig. 7, C and D), supporting the conclusion that large, M23–AQP4-enriched arrays preferentially bind to the extracellular substrate.

As interactions with the ECM mediate enrichment of AQP4 at astrocyte end-feet that surround cerebral blood vessels, experiments were done to determine if M1– and M23–AQP4 show differences in polarization toward end-feet when expressed individually. Adenovirus constructs under control of a CMV promoter show preferential expression in astrocytes when used at low titers in vivo and in vitro (Sato et al., 2004; Kuhn et al., 2011). Adenoviruses specific for M1– or M23–AQP4 were injected into the striatum of AQP4$^{-/-}$ mice, then brains were fixed and sections stained for AQP4 and for the astrocyte marker glial fibrillary acidic protein (GFAP). AQP4 labeling was imaged in isolated, GFAP-positive cells, where blood vessels could be detected by ensheathment with GFAP-labeled end-feet. Astrocytes expressing only M1–AQP4 showed diffuse AQP4 labeling throughout the cell, without obvious polarization toward blood vessels (Fig. 7 E, top), whereas astrocytes expressing only M23–AQP4 showed more restricted staining with concentration of AQP4 aggregates at end-feet adjacent to blood vessels (Fig. 7 E, bottom). Calculation of the relative density of AQP4 staining in perivascular and nonperivascular GFAP-labeled structures had a ratio of ∼1 in cells expressing M1–AQP4, whereas the ratio was >2 in cells expressing M23–AQP4 (Fig. 7 F), demonstrating significant enrichment of M23–AQP4 but not M1–AQP4 around blood vessels.

Discussion

In this study we demonstrated that the distinct aggregation properties of M1– and M23–AQP4 result in differences in their cellular localization and functions. Our principal findings are summarized in Fig. 8; they are (1) that the individually expressed AQP4 isoforms show distinct cellular localization patterns; (2) that partial segregation of M1– and M23–AQP4 occurs when they are coexpressed due to differences in diffusional mobility and substrate adhesion of small, M1-enriched versus large, M23-enriched AQP4 arrays; and (3) that differences in AQP4 isoform localization likely result in different functional roles, with M1–AQP4 required during lamellipodial extension and M23–AQP4 required for substrate interaction.

Leading-edge extension in motile cells is supported by ion transport and aquaporin-mediated water influx (Denker and Barber, 2002; Saadoun et al., 2005a). Potential mechanisms for delivery of these molecules and other integral membrane proteins such as signaling receptors and integrins to the leading edge include diffusion, vesicular delivery, bulk membrane flow, and active surface transport (Keren, 2011). Leading-edge extension is not associated with bulk membrane flow (Sheetz et al., 1989; Lee et al., 1990); instead, lipids move by Brownian motion and the membrane advances passively on both ventral and dorsal surfaces (Kucik et al., 1990). We found no evidence for directed or convective transport toward the leading edge in experiments with AQP4-GFP chimeras or in single particle–tracking experiments, where active transport or bulk membrane flow would produce an upwardly curved mean-squared displacement vs. time relationship as has been observed for β1-integrin translocation to the leading edge of migrating fibroblasts (Schmidt et al., 1993). The rate of leading-edge advance in extending lamellipodia of astrocytes and U87-MG cells is in the range 0.5–1.0 µm/min; the mean diffusional range of AQP4 is 1.7 µm in 1 min for cells expressing M1–AQP4 and 0.13 µm in 1 min for cells expressing M23–AQP4 (Crane et al., 2008). Our results demonstrate that the low plasma membrane diffusional mobility of M23–AQP4 results in exclusion from the leading edge, whereas highly mobile M1–AQP4 can freely enter extending lamellipodia. Additional factors, such as protein–protein and protein–lipid interactions, crowding, and percolation, may also be involved in the low diffusional mobility of large orthogonal arrays in the plasma membrane and contribute to the somatic retention of M23–AQP4. We have not addressed the mechanism of M1–AQP4 leading-edge enrichment in this study, but this could potentially be caused by local trapping, preferential movement perpendicular to the direction of migration once in the lamellipodium, and accumulation during multiple rounds of lamellipodial extension and retraction.

M1– and M23–AQP4 form heterotetramers when coexpressed; only M23 subunits participate in inter-tetramer associations and orthogonal arrays, with an assortment of sizes, diffusional mobilities, and M1/M23 content are found in cells expressing both isoforms (Jin et al., 2011). Our results demonstrate that size-dependent diffusion of AQP4 aggregates produces mobility-dependent sieving of small, M1–AQP4-enriched arrays into lamellipodia under these conditions. Although this

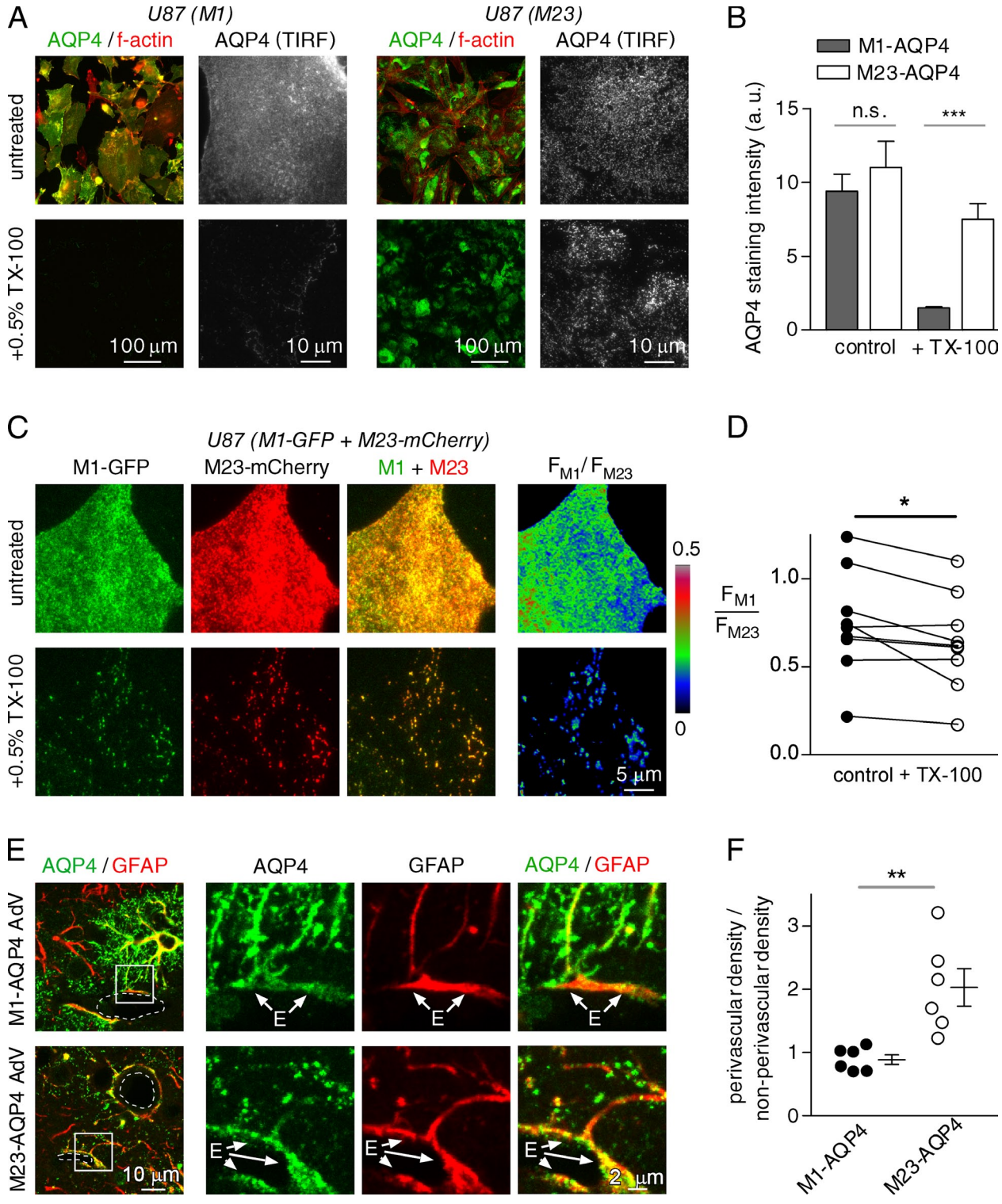

Figure 7. **ECM adhesion and polarization to astrocyte endfeet requires M23–AQP4.** (A) Wide-field and TIRF images of U87-MG cells stably transfected with M1– or M23–AQP4 and stained with antibody to AQP4 and for F-actin with phalloidin. Top panels shows untreated control cells; in bottom panels live cells were subject to detergent extraction by treatment with 0.5% Triton X-100 for 5 min before fixation. (B) Mean cellular AQP4 immunofluorescence staining intensity measured from TIRF images of M1- or M23-transfected cells under control conditions or with 0.5% Triton X-100 treatment before fixation. (n = 5 cells each, ±SE; n.s., $P > 0.05$; ***, $P < 0.001$ by t test). (C) TIRF images and ratio image of live U87-MG cells transfected with M1–AQP4–GFP and M23–AQP4–mCherry before and after incubation with 0.5% Triton X-100. (D) Quantification of M1/M23 ratio in transfected U87-MG cells before and after incubation with 0.5% Triton X-100; *, $P < 0.05$ by paired t test. (E) AQP4 distribution in astrocytes after intracerebral injection of M1– (top) or M23–AQP4 (bottom) adenoviruses into AQP4$^{-/-}$ mice. Left panels show AQP4 distribution in GFAP-labeled astrocytes adjacent to cerebral blood vessels (dotted line), right panels show an enlarged view of AQP4 and GFAP staining in astrocyte end-feet (labeled "E"). (F) Quantification of the ratio of AQP4 staining density in GFAP-labeled processes adjacent to blood vessels versus nonadjacent processes for cells transfected with M1– or M23–AQP4; **, $P < 0.01$ by t test.

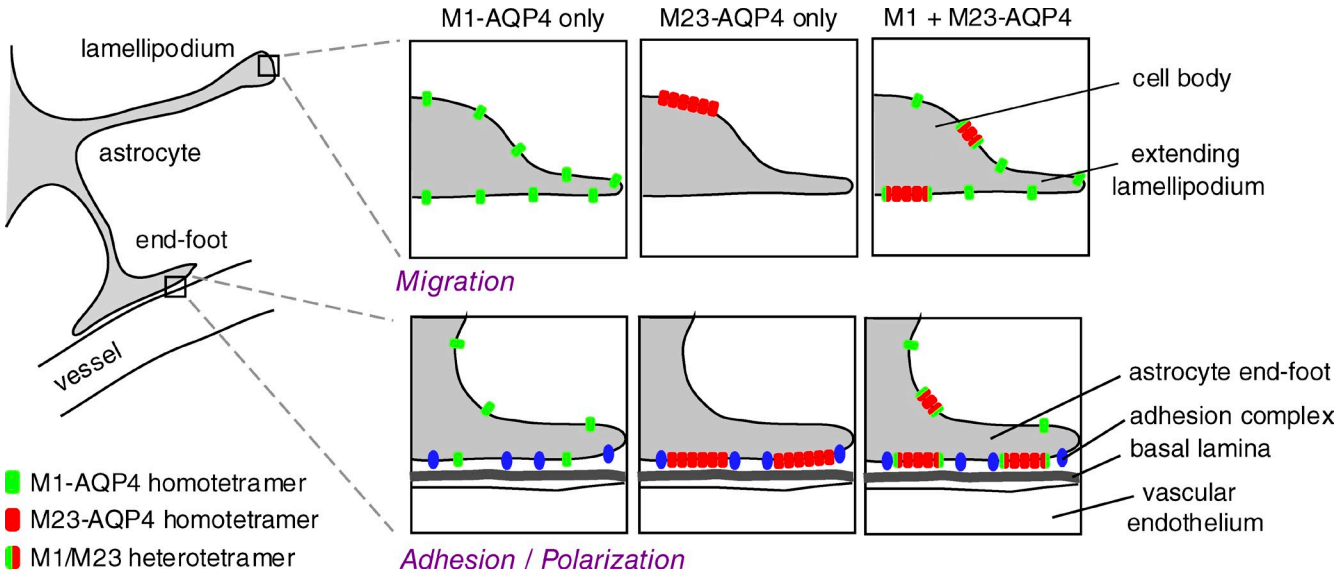

Figure 8. **Model of dynamic AQP4 segregation in astrocyte plasma membrane.** M1–AQP4 expressed individually redistributes throughout the plasma membrane and is available to diffuse into rapidly extending plasma membrane regions. M23–AQP4 expressed individually does not diffuse rapidly enough to reach protruding membrane areas, but preferentially concentrates at astrocyte end-feet due to increased affinity of large OAPs for end-foot adhesion complexes. Co-expressed M1– and M23–AQP4 form arrays of varying M1/M23 ratio, size, and diffusional mobility in which large, M23-enriched arrays are available for polarization, and small, M1-enriched arrays and single tetramers are available to support extension of peripheral astrocyte processes.

may be a unique mechanism for segregation of two isoforms of the same protein, mobility-dependent sieving might be a more general mechanism to segregate molecules that display physiologically regulated plasma membrane mobility, such as integrin nanoclusters (Bakker et al., 2012) and immunoglobulin receptor complexes (Jaumouillé and Grinstein, 2011). Regulation of surface mobility is therefore a mechanism that can allow cells to specify which plasma membrane proteins can access rapidly extending membrane regions such as lamellipodia, filopodia, or phagocytic cups.

The finding that M1–AQP4 but not M23–AQP4 increases lamellipodial stability and facilitates cell migration demonstrates the importance of leading-edge localization of AQP4 in motile cells. The requirement for this localized water flux presumably reflects the localization of transmembrane osmotic pressure gradients generated by activation of ion channels or exchangers at the leading edge. Cytosolic hydrostatic pressure equilibrates slowly over distance relevant to lamellipodial extension (Charras et al., 2005), so the subcellular localization of water influx may be important during leading-edge extension even under conditions where transmembrane osmotic gradients are more diffusely localized. The mechanisms connecting AQP4 to lamellipodial stability are presently unknown; maintenance of stability requires continual delivery of actin monomers to the leading edge (Lee et al., 2013), and leading-edge water influx may assist diffusion of actin monomers by decreasing crowding within the lamellipodial cytoplasm. Similar relationships between lamellipodial stability and cell migration rate have been observed after knockdown of other proteins such as p120 catenin (Boguslavsky et al., 2007), PAK1 (Smith et al., 2008), and actinin-4 (Hamill et al., 2013), and are consistent with models of cell migration that emphasize the importance of the lamellipodium in directed cellular movement (Petrie et al., 2009).

In addition to different roles of M1– versus M23–AQP4 in cell migration, we demonstrate differential interaction with extracellular substrate and different roles in localization to astrocyte end-feet. The simplest explanation for these findings is that the aggregation of M23–AQP4 into large orthogonal arrays of >100 tetramers increases avidity for extracellular substrate by increasing the number of sites available to interact with adhesion complexes. The exact nature of the molecular interactions responsible for AQP4 substrate binding and polarization remain unclear. The loss of AQP4 polarization observed in α-syntrophin knockout mice (Neely et al., 2001) led to the hypothesis that binding of AQP4 to the dystrophin complex mediates anchoring to the basal lamina surrounding blood vessels. However, we found substantial immobilization of C-terminal M23–AQP4–GFP fusion proteins, in which the consensus PDZ-binding domain is presumably blocked from interaction with the α-syntrophin PDZ domain. Recent findings suggest that AQP4 polarization may involve additional or alternative factors, as subsets of macroglia retain AQP4 polarization in the absence of α-syntrophin (Enger et al., 2012) and AQP4 interaction with extracellular substrates is sensitive to disruption of integrin function (Tham and Moukhles, 2011). Vesicular trafficking might also play a role in redistribution of AQP4 in cultured astrocytes (Potokar et al., 2013), but it remains unclear if directed trafficking toward end-feet contributes to AQP4 polarization in situ. Enrichment of AQP4 at astrocyte end-feet is required for rapid water transport across the blood–brain barrier and the loss of polarization observed in several neurological conditions, including Alzheimer's disease (Wilcock et al., 2009) and after ischemia (Landis and Reese, 1981; Frydenlund et al., 2006), may contribute to pathology. Our finding that M23–AQP4-dependent formation of orthogonal arrays is required for localization to end-feet may lead to a

more complete mechanistic understanding of polarization loss in these conditions.

This study is the first to identify isoform-specific requirements for M1– or M23–AQP4 and we would predict further functional requirements for each isoform on the basis of the differences in their subcellular localization. AQP4 facilitates K^+ clearance by astrocytes after neuronal activity (Amiry-Moghaddam et al., 2003; Padmawar et al., 2005); current models propose that this is caused by coupling of K^+ uptake to swelling of fine astrocytic processes in the neuropil (Jin et al., 2013) and would therefore require M1–AQP4 expression. Projection of astrocyte lamellipodial processes toward active synapses in acute brain slices (Hirrlinger et al., 2004) may depend on AQP4-mediated water influx (Reichenbach et al., 2010); our results would predict that this process is M1–AQP4 dependent. M23–AQP4-mediated polarization to astrocyte end-feet is predicted to be associated with AQP4-dependent increases in water influx during cytotoxic edema and increases in the rate of clearance after vasogenic edema (Manley et al., 2000; Papadopoulos et al., 2004). In addition to the M1– and M23–AQP4 isoforms, several additional AQP4 transcripts have been identified in rat brain mRNA preparations (Moe et al., 2008), one of which (Mz-AQP4) is translated at low levels in rat brain lysates (Rossi et al., 2011). Rat Mz-AQP4 shows similar biochemical properties to M1–AQP4 and we would predict similar functional roles for this isoform; however, as Mz-AQP4 is not expressed in human or mouse brain (Rossi et al., 2011) it would not affect the results reported in this study.

The differential expression and supramolecular organization of M1– and M23–AQP4 isoforms provides a mechanism by which AQP4 can be locally enriched in specific subcellular regions but remain available for rapid translocation into extending membrane structures. It remains to be determined if alterations in the M1/M23 ratio occur in physiologically relevant situations. Individual M1– and M23–AQP4 transcripts are generated from separate promoters in the AQP4 gene, and differences in isoform expression after vasopressin treatment (Van Hoek et al., 2009) as well as differential regulation by microRNAs (Sepramaniam et al., 2012) have been reported. Astrocytes cultured in vitro using conventional methods show gene expression profiles similar to those associated with reactive astrocytes (Foo et al., 2011) and display a very different M1/M23 ratio than that observed in vivo (1:1 vs. 1:3), supporting the possibility that M1/M23 ratio is subject to physiological regulation.

In conclusion, our results suggest specific biological roles for two distinct AQP4 isoforms. The association of AQP4 isoforms into supramolecular aggregates of different size and composition allow individual astrocytes to carry out their major functions, including migration and adhesion/polarization, without altering global membrane water permeability.

Materials and methods

Materials

Culture and brain-slice immunostaining was done using an anti-AQP4 C-terminal rabbit polyclonal antibody (Santa Cruz Biotechnology, Inc.), with recombinant monoclonal antibodies derived from NMO patients (Bennett et al., 2009) or with mouse monoclonal GFAP antibody (EMD Millipore). M1–AQP4 and M23–AQP4 were expressed from plasmid pcDNA3.1 under control of the CMV immediate early promoter (Tajima et al., 2010). M1–AQP4–GFP, M23–AQP4–GFP, and M23–AQP4–mCherry (Rossi et al., 2012c) were expressed from plasmids pEGFP-N1 or pmCherry-N1 under control of the CMV immediate early promoter. LifeAct-mCherry plasmid was generated by PCR amplification of the LifeAct cDNA (Riedl et al., 2008) and cloning into pmCherry-N1 (Takara Bio Inc.). M1–AQP4 and M23–AQP4 adenovirus vectors (Li et al., 2011) were generated by Vector BioLabs from M1–AQP4 and M23–AQP4 subcloned into adenoviral shuttle vector pDual-CCM under control of the CMV immediate early promoter. Alexa Fluor dye and quantum dot–conjugated secondary antibodies, phalloidin, and FITC-conjugated wheat germ agglutinin, were from Life Technologies.

Cell culture and transfection

U87-MG glioblastoma cells (ATCC, Manassas, VA) were maintained in DMEM H-21/10% FBS and passaged twice weekly. Transient plasmid transfections were done with Lipofectamine 2000 (Invitrogen) according to the manufacturer's instructions. After 16 h, transfection media was replaced and cells were trypsinized and re-plated on fibronectin-coated glass coverslips (Neuvitro) at low density (50 cells/mm^2). Cells were then allowed to recover for 24 h before use in imaging experiments. U87-MG clones stably transfected with M1– or M23–AQP4 (Crane et al., 2011) were generated from cells transfected with pcDNA3.1 vectors that were subsequently cloned at very low density in 96-well plates and selected for geneticin resistance. Primary cultures of mouse astrocytes were generated from the cortex of $AQP4^{+/+}$ and $AQP4^{-/-}$ mice at P0 using standard techniques (Crane et al., 2009). Cells were grown in tissue culture flasks for 7–10 d in DMEM H-16/10% FBS, then trypsinized and re-plated on poly-D-lysine–coated glass coverslips at a density of 10^3 cells/mm^2 and used for experiments after 14–21 d. Cell monolayers were infected with adenovirus containing M1–AQP4 or M23–AQP4 expression constructs (Li et al., 2011) at 4×10^7 cfu/ml for 24 h, media was then changed, monolayers were scratched with a plastic pipette tip, and astrocytes were allowed to migrate back into the scratch wound for 16 h.

TIRF and *d*STORM imaging

Cells were fixed for 30 min with 4% paraformaldehyde in PBS (pH 7.4) followed by permeabilization and staining with primary then secondary antibodies, wheat germ agglutinin, or phalloidin conjugates. In experiments where AQP4 extracellular epitopes were stained with recombinant NMO-IgG, antibodies were applied to the media at 10 µg/ml for 10 min, then unbound antibody was washed with three changes of HBSS/Hepes before fixation and subsequent processing. In live-cell imaging experiments, U87-MG cells were plated on 25-mm fibronectin-coated coverslips and experiments were done in an open bath incubator at 35°C in DMEM/FBS superfused with 5% CO_2/95% O_2. Fixed cells were imaged in PBS. TIRF imaging of stained and live cells was performed on an inverted microscope (model TE-2000E; Nikon) equipped with 100×/1.49 NA objective, autofocus unit, four diode lasers for excitation (405, 488, 561, and 642 nm) under AOTF control (AA Optoelectronic), quad-band filter cube and appropriate emission filters (Semrock) mounted on a Lambda 10-3 optical filter changer (Sutter Instrument), and EM-CCD camera (QuantEM:512SC; Photometrics) under control of Micro-Manager 1.3/1.4 software (Edelstein et al., 2010). In experiments where M1-GFP and M23-mCherry were co-expressed, significant (24%) FRET-dependent quenching of the GFP signal was revealed by acceptor photobleaching. To prevent inaccuracies due to differences in GFP quenching between soma and lamellipodia, we first acquired an mCherry image, and then completely photobleached mCherry with the 561-nm laser at full power for 2 min before acquisition of the GFP image. For *d*STORM, cells were fixed and stained as above with anti–C-terminal AQP4 antibody, Alexa Fluor 647–labeled secondary antibody, Alexa Fluor 488–phalloidin, and 0.1 µm TetraSpeck fluorescent microspheres (Life Technologies) as fiducial markers. Single images showing distribution of F-actin and AQP4 were captured, then Alexa Fluor 647 was switched to dark state by incubation of fixed cells with 100 mM β-mercaptoethylamine (MEA; Sigma-Aldrich) in PBS at pH 9.0 and increase of laser power (van de Linde et al., 2011). Spontaneous reactivation of individual fluorophores was measured over 10–20,000 frames, and detection and localization of individual fluorophores, drift correction, and image reconstruction was performed with the QuickPALM plugin for ImageJ (National Institutes of Health, Bethesda, MD; Henriques et al., 2010). Reconstructed images were rendered with 10-nm pixels and filtered with a 30-nm-diameter Gaussian blur function. For estimation of array size, a 1-pixel radius median filter was applied to improve edge definition and arrays were then

detected by binary thresholding and particle analysis in ImageJ. Lamellipodial protrusions were identified by actin staining and particles were subsequently classified as lamellipodial or somatic based on position. The fraction of AQP4 in aggregates of a given size was calculated by multiplying aggregate area by the corresponding number of aggregates, and normalizing to total AQP4 staining area in the cellular region under consideration.

Quantum dot, single-particle tracking

AQP4 was labeled in live astrocytes by a 5-min incubation with mAb r58 at 0.2 µg/ml followed by 0.2 µg/ml QD655-conjugated goat anti–human secondary antibody in phenol red/FBS-free DMEM containing 10 mM Hepes. Experiments were done in phenol red–free DMEM with 10% FBS and 10 mM Hepes at 35°C on an inverted microscope (model TE-2000S; Nikon) equipped with stage incubator, shuttered lamp, and 100×/1.3 NA Ph3 oil objective. Image sequences were acquired with an EM-CCD camera (Hamamtsu Photonics) using Wasabi software. Phase-contrast images, which were used for assignment of reconstructed tracks to lamellipodial or somatic regions, were obtained immediately before 10-s image series at 30 Hz for reconstruction of single-particle trajectories. Tracks that crossed between these regions were excluded from analysis. Reconstruction of particle tracks was performed using the IDL macros for particle tracking (Crocker and Grier, 1996) and Labview MSD analysis macro (Crane et al., 2008).

Mathematical modeling

AQP4 diffusional sieving was modeled here, building on our prior model of the number distributions of OAP size and composition as a function M1/M23 ratio (Jin et al., 2011), which assumed random tetrameric assembly of M1 and M23, inter-tetramer associations between M23 and M23, and a free energy constraint limiting OAP size. To model diffusional sieving, 10^5–10^6 OAPs were generated at specified M1/M23 ratio, with each OAP assigned a diffusion coefficient, $D(n) = 0.029 \times e^{(-0.067n)} + 2.4 \times 10^{-4}$ ($\mu m^2/s$), where n is the number of tetramers per orthogonal array, which was based on experimental data (see Fig. 5 A). Particle diffusion was simulated by Brownian dynamics using MATLAB (The MathWorks). Each array was initially distributed randomly in a 50 × 50-µm, two-dimensional cell body. At each time step, *x* and *y* displacements were specified by random diffusion, using a random generation function with zero mean and standard deviation $(2D(n)\Delta t)^{1/2}$, where the $D(n)$ is OAP size-dependent diffusion coefficient and Δt is the time step. Particles moving outside of the cell boundary were reflected using reflective boundary condition. Lamellipodial extension was modeled by continuous expansion of the leading edge with linear velocity 0.5 µm/min over 10 min, allowing diffusion of AQP4 particles into the newly created space. Computed results included single-particle trajectories, as well as distributions (and average) particle concentration, size, and M1/M23 composition in lamellipodia vs. nonlamellipodial cell body.

Cell migration assays

Transwell migration of U87-MG cells stably transfected with M1– or M23–AQP4 was performed essentially as described previously (Saadoun et al., 2005b). 5×10^4 cells in DMEM containing 1% FBS were plated on polycarbonate membranes with 8-µm-diameter pores (Costar) and allowed to migrate across the pores into media containing 1% or 10% FBS for 16 h. After migration cells were fixed and stained with Coomassie, nonmigrated cells were removed by scraping with a cotton bud. Membranes were then photographed and cells were subsequently lysed with 1% Triton X-100 and retained dye was quantified by spectrophotometry. The percentage of cells that had migrated was determined by comparison to membranes in which nonmigrated cells were not removed. Background from membranes in which cells were removed from both sides of the membrane was subtracted. Lamellipodial dynamics of astrocytes migrating in phenol red–free DMEM with 10% FBS and 10 mM Hepes at 37°C were recorded by phase-contrast video microscopy using an inverted microscope (Eclipse Ti; Nikon) equipped with stage incubator, a 100×/NA 1.3 Ph3 objective, and a camera (Clara; Andor Technology) controlled by NIS elements software (Nikon). Kymograms were generated by sectioning sequences along a line drawn perpendicular to the center of the advancing lamellipodium using ImageJ software and analyzed manually as described previously (Hinz et al., 1999).

Adhesion and polarization assays

AQP4–substrate interactions were assayed by allowing U87-MG cells transfected with M1– or M23–AQP4 to adhere to fibronectin-coated coverslips for 24 h, then incubating the cells with 0.5% Triton X-100 for 5 min followed by extensive washing, fixation, and staining for AQP4 and phalloidin. The average AQP4 cellular fluorescence in TIRF images was expressed as a fraction of the average intensity in cells that were not solubilized before fixation. Polarization of AQP4 to astrocyte end-feet was determined by intracerebral injection of adenoviruses into $AQP4^{-/-}$ mice. All animal studies were approved by the UCSF Institutional Animal Care and Use Committee (IACUC). Mice were anesthetized and mounted on a stereotactic frame. A midline scalp incision was made and a burr hole of 1-mm diameter was drilled in the skull 2 mm to the right of the bregma. A 30-gauge needle attached to a 50-µl gas-tight glass syringe (Hamilton) was inserted in the striatum 3 mm deep to infuse 8 µl adenovirus solution (~1 µl/min). Mice were sacrificed after 7 d and brains were processed for sectioning. 5-µm-thick paraffin sections were deparaffinized with xylene, rehydrated, then blocked for 1 h in PBS containing 1% BSA and 0.1% Triton X-100, incubated for 1 h at room temperature with the indicated primary antibodies, washed with PBS, and incubated for 1 h with Alexa Fluor 488– or 555–conjugated secondary antibodies (1:1,000; Life Technologies). Sections were then washed with PBS and mounted in ProLong Gold Antifade (Life Technologies). Sections were imaged using a laser-scanning confocal microscope (Eclipse C1; Nikon) equipped with a 100×/NA 1.49 objective lens under control of EZ-C1 software (Nikon). For analysis, a threshold was applied to AQP4 and GFAP channels and the fraction of GFAP-labeled structures that were also stained for AQP4 was computed for perivascular and nonperivascular regions.

Online supplemental material

Video 1 shows distribution of M1–AQP4–GFP and LifeAct mCherry–labeled F-actin in transiently transfected U87-MG cells migrating on fibronectin-coated coverslips. Video 2 shows the same experiment but in cells transfected with M23–AQP4–GFP instead of M1–AQP4–GFP. Video 3 shows distribution of M1–AQP4–GFP and M23–AQP4–mCherry in migrating U87-MG cells cotransfected with both constructs. Videos 4 and 5 show simulations of orthogonal array diffusion into lamellipodia at M1–AQP4/M23–AQP4 ratios of 1:1 and 1:3, respectively. Video 6 shows leading-edge dynamics of wild-type and $AQP4^{-/-}$ astrocytes during migration into a scratch wound. Online supplemental material is available at http://www.jcb.org/cgi/content/full/jcb.201308118/DC1.

We thank A. Rossi and P. Haggie for technical assistance and informative discussions.

This work was supported by grants EB00415, DK35124, EY13574, DK86125, and DK72517 from the National Institutes of Health and a grant from the Guthy-Jackson Charitable Foundation.

The authors declare no competing financial interests.

Submitted: 20 August 2013
Accepted: 20 December 2013

References

Amiry-Moghaddam, M., A. Williamson, M. Palomba, T. Eid, N.C. de Lanerolle, E.A. Nagelhus, M.E. Adams, S.C. Froehner, P. Agre, and O.P. Ottersen. 2003. Delayed K^+ clearance associated with aquaporin-4 mislocalization: phenotypic defects in brains of alpha-syntrophin-null mice. *Proc. Natl. Acad. Sci. USA*. 100:13615–13620. http://dx.doi.org/10.1073/pnas.2336064100

Auguste, K.I., S. Jin, K. Uchida, D. Yan, G.T. Manley, M.C. Papadopoulos, and A.S. Verkman. 2007. Greatly impaired migration of implanted aquaporin-4-deficient astroglial cells in mouse brain toward a site of injury. *FASEB J.* 21:108–116. http://dx.doi.org/10.1096/fj.06-6848com

Bakker, G.J., C. Eich, J.A. Torreno-Pina, R. Diez-Ahedo, G. Perez-Samper, T.S. van Zanten, C.G. Figdor, A. Cambi, and M.F. Garcia-Parajo. 2012. Lateral mobility of individual integrin nanoclusters orchestrates the onset for leukocyte adhesion. *Proc. Natl. Acad. Sci. USA*. 109:4869–4874. http://dx.doi.org/10.1073/pnas.1116425109

Bennett, J.L., C. Lam, S.R. Kalluri, P. Saikali, K. Bautista, C. Dupree, M. Glogowska, D. Case, J.P. Antel, G.P. Owens, et al. 2009. Intrathecal pathogenic anti-aquaporin-4 antibodies in early neuromyelitis optica. *Ann. Neurol.* 66:617–629. http://dx.doi.org/10.1002/ana.21802

Binder, D.K., X. Yao, Z. Zador, T.J. Sick, A.S. Verkman, and G.T. Manley. 2006. Increased seizure duration and slowed potassium kinetics in mice lacking aquaporin-4 water channels. *Glia*. 53:631–636. http://dx.doi.org/10.1002/glia.20318

Boguslavsky, S., I. Grosheva, E. Landau, M. Shtutman, M. Cohen, K. Arnold, E. Feinstein, B. Geiger, and A. Bershadsky. 2007. p120 catenin regulates lamellipodial dynamics and cell adhesion in cooperation with cortactin. *Proc. Natl. Acad. Sci. USA*. 104:10882–10887. http://dx.doi.org/10.1073/pnas.0702731104

Boiko, T., M. Vakulenko, H. Ewers, C.C. Yap, C. Norden, and B. Winckler. 2007. Ankyrin-dependent and -independent mechanisms orchestrate axonal compartmentalization of L1 family members neurofascin and L1/neuron-glia cell adhesion molecule. *J. Neurosci.* 27:590–603. http://dx.doi.org/10.1523/JNEUROSCI.4302-06.2007

Caspani, E.M., D. Echevarria, K. Rottner, and J.V. Small. 2006. Live imaging of glioblastoma cells in brain tissue shows requirement of actin bundles for migration. *Neuron Glia Biol.* 2:105–114. http://dx.doi.org/10.1017/S1740925X06000111

Charras, G.T., J.C. Yarrow, M.A. Horton, L. Mahadevan, and T.J. Mitchison. 2005. Non-equilibration of hydrostatic pressure in blebbing cells. *Nature*. 435:365–369. http://dx.doi.org/10.1038/nature03550

Crane, J.M., and A.S. Verkman. 2009. Determinants of aquaporin-4 assembly in orthogonal arrays revealed by live-cell single-molecule fluorescence imaging. *J. Cell Sci.* 122:813–821. http://dx.doi.org/10.1242/jcs.042341

Crane, J.M., A.N. Van Hoek, W.R. Skach, and A.S. Verkman. 2008. Aquaporin-4 dynamics in orthogonal arrays in live cells visualized by quantum dot single particle tracking. *Mol. Biol. Cell*. 19:3369–3378. http://dx.doi.org/10.1091/mbc.E08-03-0322

Crane, J.M., J.L. Bennett, and A.S. Verkman. 2009. Live cell analysis of aquaporin-4 m1/m23 interactions and regulated orthogonal array assembly in glial cells. *J. Biol. Chem.* 284:35850–35860. http://dx.doi.org/10.1074/jbc.M109.071670

Crane, J.M., C. Lam, A. Rossi, T. Gupta, J.L. Bennett, and A.S. Verkman. 2011. Binding affinity and specificity of neuromyelitis optica autoantibodies to aquaporin-4 M1/M23 isoforms and orthogonal arrays. *J. Biol. Chem.* 286:16516–16524. http://dx.doi.org/10.1074/jbc.M111.227298

Crocker, J.C., and D.G. Grier. 1996. Methods of digital video microscopy for colloidal studies. *J. Colloid Interface Sci.* 179:298–310. http://dx.doi.org/10.1006/jcis.1996.0217

Denker, S.P., and D.L. Barber. 2002. Cell migration requires both ion translocation and cytoskeletal anchoring by the Na-H exchanger NHE1. *J. Cell Biol.* 159:1087–1096. http://dx.doi.org/10.1083/jcb.200208050

Edelstein, A., N. Amodaj, K. Hoover, R. Vale, and N. Stuurman. 2010. Computer control of microscopes using microManager. *Curr. Protoc. Mol. Biol.* Chapter 14:Unit14.20.

Enger, R., G.A. Gundersen, N.N. Haj-Yasein, M. Eilert-Olsen, A.E. Thoren, G.F. Vindedal, P.H. Petersen, O. Skare, M. Nedergaard, O.P. Ottersen, and E.A. Nagelhus. 2012. Molecular scaffolds underpinning macroglial polarization: an analysis of retinal Müller cells and brain astrocytes in mouse. *Glia*. 60:2018–2026. http://dx.doi.org/10.1002/glia.22416

Foo, L.C., N.J. Allen, E.A. Bushong, P.B. Ventura, W.S. Chung, L. Zhou, J.D. Cahoy, R. Daneman, H. Zong, M.H. Ellisman, and B.A. Barres. 2011. Development of a method for the purification and culture of rodent astrocytes. *Neuron*. 71:799–811. http://dx.doi.org/10.1016/j.neuron.2011.07.022

Frydenlund, D.S., A. Bhardwaj, T. Otsuka, M.N. Mylonakou, T. Yasumura, K.G. Davidson, E. Zeynalov, O. Skare, P. Laake, F.M. Haug, et al. 2006. Temporary loss of perivascular aquaporin-4 in neocortex after transient middle cerebral artery occlusion in mice. *Proc. Natl. Acad. Sci. USA*. 103:13532–13536. http://dx.doi.org/10.1073/pnas.0605796103

Furman, C.S., D.A. Gorelick-Feldman, K.G. Davidson, T. Yasumura, J.D. Neely, P. Agre, and J.E. Rash. 2003. Aquaporin-4 square array assembly: opposing actions of M1 and M23 isoforms. *Proc. Natl. Acad. Sci. USA*. 100:13609–13614. http://dx.doi.org/10.1073/pnas.2235843100

Hamill, K.J., S.B. Hopkinson, O. Skalli, and J.C. Jones. 2013. Actinin-4 in keratinocytes regulates motility via an effect on lamellipodia stability and matrix adhesions. *FASEB J.* 27:546–556. http://dx.doi.org/10.1096/fj.12-217406

Henriques, R., M. Lelek, E.F. Fornasiero, F. Valtorta, C. Zimmer, and M.M. Mhlanga. 2010. QuickPALM: 3D real-time photoactivation nanoscopy image processing in ImageJ. *Nat. Methods*. 7:339–340. http://dx.doi.org/10.1038/nmeth0510-339

Hinz, B., W. Alt, C. Johnen, V. Herzog, and H.W. Kaiser. 1999. Quantifying lamella dynamics of cultured cells by SACED, a new computer-assisted motion analysis. *Exp. Cell Res.* 251:234–243. http://dx.doi.org/10.1006/excr.1999.4541

Hirrlinger, J., S. Hülsmann, and F. Kirchhoff. 2004. Astroglial processes show spontaneous motility at active synaptic terminals in situ. *Eur. J. Neurosci.* 20:2235–2239. http://dx.doi.org/10.1111/j.1460-9568.2004.03689.x

Jaumouillé, V., and S. Grinstein. 2011. Receptor mobility, the cytoskeleton, and particle binding during phagocytosis. *Curr. Opin. Cell Biol.* 23:22–29. http://dx.doi.org/10.1016/j.ceb.2010.10.006

Jin, B.J., A. Rossi, and A.S. Verkman. 2011. Model of aquaporin-4 supramolecular assembly in orthogonal arrays based on heterotetrameric association of M1-M23 isoforms. *Biophys. J.* 100:2936–2945. http://dx.doi.org/10.1016/j.bpj.2011.05.012

Jin, B.J., H. Zhang, D.K. Binder, and A.S. Verkman. 2013. Aquaporin-4-dependent K(+) and water transport modeled in brain extracellular space following neuroexcitation. *J. Gen. Physiol.* 141:119–132. http://dx.doi.org/10.1085/jgp.201210883

Jung, J.S., R.V. Bhat, G.M. Preston, W.B. Guggino, J.M. Baraban, and P. Agre. 1994. Molecular characterization of an aquaporin cDNA from brain: candidate osmoreceptor and regulator of water balance. *Proc. Natl. Acad. Sci. USA*. 91:13052–13056. http://dx.doi.org/10.1073/pnas.91.26.13052

Keren, K. 2011. Cell motility: the integrating role of the plasma membrane. *Eur. Biophys. J.* 40:1013–1027. http://dx.doi.org/10.1007/s00249-011-0741-0

Kucik, D.F., E.L. Elson, and M.P. Sheetz. 1990. Cell migration does not produce membrane flow. *J. Cell Biol.* 111:1617–1622. http://dx.doi.org/10.1083/jcb.111.4.1617

Kuhn, B., T.M. Hoogland, and S.S. Wang. 2011. Injection of recombinant adenovirus for delivery of genetically encoded calcium indicators into astrocytes of the cerebellar cortex. *Cold Spring Harb Protoc*. 2011:1217–1223. http://dx.doi.org/10.1101/pdb.prot065797

Landis, D.M., and T.S. Reese. 1974. Arrays of particles in freeze-fractured astrocytic membranes. *J. Cell Biol.* 60:316–320. http://dx.doi.org/10.1083/jcb.60.1.316

Landis, D.M., and T.S. Reese. 1981. Astrocyte membrane structure: changes after circulatory arrest. *J. Cell Biol.* 88:660–663. http://dx.doi.org/10.1083/jcb.88.3.660

Lee, C.W., E.A. Vitriol, S. Shim, A.L. Wise, R.P. Velayutham, and J.Q. Zheng. 2013. Dynamic localization of G-actin during membrane protrusion in neuronal motility. *Curr. Biol.* 23:1046–1056. http://dx.doi.org/10.1016/j.cub.2013.04.057

Lee, J., M. Gustafsson, K.E. Magnusson, and K. Jacobson. 1990. The direction of membrane lipid flow in locomoting polymorphonuclear leukocytes. *Science*. 247:1229–1233. http://dx.doi.org/10.1126/science.2315695

Li, L., H. Zhang, M. Varrin-Doyer, S.S. Zamvil, and A.S. Verkman. 2011. Proinflammatory role of aquaporin-4 in autoimmune neuroinflammation. *FASEB J.* 25:1556–1566. http://dx.doi.org/10.1096/fj.10-177279

Lu, M., M.D. Lee, B.L. Smith, J.S. Jung, P. Agre, M.A. Verdijk, G. Merkx, J.P. Rijss, and P.M. Deen. 1996. The human AQP4 gene: definition of the locus encoding two water channel polypeptides in brain. *Proc. Natl. Acad. Sci. USA*. 93:10908–10912. http://dx.doi.org/10.1073/pnas.93.20.10908

Manley, G.T., M. Fujimura, T. Ma, N. Noshita, F. Filiz, A.W. Bollen, P. Chan, and A.S. Verkman. 2000. Aquaporin-4 deletion in mice reduces brain edema after acute water intoxication and ischemic stroke. *Nat. Med.* 6:159–163. http://dx.doi.org/10.1038/72256

McCoy, E., and H. Sontheimer. 2007. Expression and function of water channels (aquaporins) in migrating malignant astrocytes. *Glia*. 55:1034–1043. http://dx.doi.org/10.1002/glia.20524

Moe, S.E., J.G. Sorbo, R. Sogaard, T. Zeuthen, O. Petter Ottersen, and T. Holen. 2008. New isoforms of rat Aquaporin-4. *Genomics*. 91:367–377. http://dx.doi.org/10.1016/j.ygeno.2007.12.003

Neely, J.D., B.M. Christensen, S. Nielsen, and P. Agre. 1999. Heterotetrameric composition of aquaporin-4 water channels. *Biochemistry*. 38:11156–11163. http://dx.doi.org/10.1021/bi990941s

Neely, J.D., M. Amiry-Moghaddam, O.P. Ottersen, S.C. Froehner, P. Agre, and M.E. Adams. 2001. Syntrophin-dependent expression and localization of Aquaporin-4 water channel protein. *Proc. Natl. Acad. Sci. USA*. 98:14108–14113. http://dx.doi.org/10.1073/pnas.241508198

Nielsen, S., E.A. Nagelhus, M. Amiry-Moghaddam, C. Bourque, P. Agre, and O.P. Ottersen. 1997. Specialized membrane domains for water transport in glial cells: high-resolution immunogold cytochemistry of aquaporin-4 in rat brain. *J. Neurosci.* 17:171–180.

Padmawar, P., X. Yao, O. Bloch, G.T. Manley, and A.S. Verkman. 2005. K^+ waves in brain cortex visualized using a long-wavelength K+-sensing fluorescent indicator. *Nat. Methods*. 2:825–827. http://dx.doi.org/10.1038/nmeth801

Papadopoulos, M.C., and A.S. Verkman. 2013. Aquaporin water channels in the nervous system. *Nat. Rev. Neurosci.* 14:265–277. http://dx.doi.org/10.1038/nrn3468

Papadopoulos, M.C., G.T. Manley, S. Krishna, and A.S. Verkman. 2004. Aquaporin-4 facilitates reabsorption of excess fluid in vasogenic brain edema. *FASEB J.* 18:1291–1293.

Petrie, R.J., A.D. Doyle, and K.M. Yamada. 2009. Random versus directionally persistent cell migration. *Nat. Rev. Mol. Cell Biol.* 10:538–549. http://dx.doi.org/10.1038/nrm2729

Potokar, M., M. Stenovec, J. Jorgačevski, T. Holen, M. Kreft, O.P. Ottersen, and R. Zorec. 2013. Regulation of AQP4 surface expression via vesicle mobility in astrocytes. *Glia*. 61:917–928. http://dx.doi.org/10.1002/glia.22485

Reichenbach, A., A. Derouiche, and F. Kirchhoff. 2010. Morphology and dynamics of perisynaptic glia. *Brain Res. Brain Res. Rev.* 63:11–25. http://dx.doi.org/10.1016/j.brainresrev.2010.02.003

Riedl, J., A.H. Crevenna, K. Kessenbrock, J.H. Yu, D. Neukirchen, M. Bista, F. Bradke, D. Jenne, T.A. Holak, Z. Werb, et al. 2008. Lifeact: a versatile marker to visualize F-actin. *Nat. Methods*. 5:605–607. http://dx.doi.org/10.1038/nmeth.1220

Rossi, A., J.M. Crane, and A.S. Verkman. 2011. Aquaporin-4 Mz isoform: brain expression, supramolecular assembly and neuromyelitis optica antibody binding. *Glia*. 59:1056–1063. http://dx.doi.org/10.1002/glia.21177

Rossi, A., F. Baumgart, A.N. van Hoek, and A.S. Verkman. 2012a. Post-Golgi supramolecular assembly of aquaporin-4 in orthogonal arrays. *Traffic*. 13:43–53. http://dx.doi.org/10.1111/j.1600-0854.2011.01299.x

Rossi, A., T.J. Moritz, J. Ratelade, and A.S. Verkman. 2012b. Super-resolution imaging of aquaporin-4 orthogonal arrays of particles in cell membranes. *J. Cell Sci.* 125:4405–4412. http://dx.doi.org/10.1242/jcs.109603

Rossi, A., J. Ratelade, M.C. Papadopoulos, J.L. Bennett, and A.S. Verkman. 2012c. Neuromyelitis optica IgG does not alter aquaporin-4 water permeability, plasma membrane M1/M23 isoform content, or supramolecular assembly. *Glia*. 60:2027–2039. http://dx.doi.org/10.1002/glia.22417

Saadoun, S., M.C. Papadopoulos, D.C. Davies, S. Krishna, and B.A. Bell. 2002. Aquaporin-4 expression is increased in oedematous human brain tumours. *J. Neurol. Neurosurg. Psychiatry*. 72:262–265. http://dx.doi.org/10.1136/jnnp.72.2.262

Saadoun, S., M.C. Papadopoulos, M. Hara-Chikuma, and A.S. Verkman. 2005a. Impairment of angiogenesis and cell migration by targeted aquaporin-1 gene disruption. *Nature*. 434:786–792. http://dx.doi.org/10.1038/nature03460

Saadoun, S., M.C. Papadopoulos, H. Watanabe, D. Yan, G.T. Manley, and A.S. Verkman. 2005b. Involvement of aquaporin-4 in astroglial cell migration and glial scar formation. *J. Cell Sci.* 118:5691–5698. http://dx.doi.org/10.1242/jcs.02680

Sato, Y., Y. Shiraishi, and T. Furuichi. 2004. Cell specificity and efficiency of the Semliki forest virus vector- and adenovirus vector-mediated gene expression in mouse cerebellum. *J. Neurosci. Methods*. 137:111–121. http://dx.doi.org/10.1016/j.jneumeth.2004.02.014

Schmidt, C.E., A.F. Horwitz, D.A. Lauffenburger, and M.P. Sheetz. 1993. Integrin-cytoskeletal interactions in migrating fibroblasts are dynamic, asymmetric, and regulated. *J. Cell Biol.* 123:977–991. http://dx.doi.org/10.1083/jcb.123.4.977

Sepramaniam, S., L.K. Ying, A. Armugam, E.M. Wintour, and K. Jeyaseelan. 2012. MicroRNA-130a represses transcriptional activity of aquaporin 4 M1 promoter. *J. Biol. Chem.* 287:12006–12015. http://dx.doi.org/10.1074/jbc.M111.280701

Sheetz, M.P., S. Turney, H. Qian, and E.L. Elson. 1989. Nanometre-level analysis demonstrates that lipid flow does not drive membrane glycoprotein movements. *Nature*. 340:284–288. http://dx.doi.org/10.1038/340284a0

Smith, S.D., Z.M. Jaffer, J. Chernoff, and A.J. Ridley. 2008. PAK1-mediated activation of ERK1/2 regulates lamellipodial dynamics. *J. Cell Sci.* 121:3729–3736. http://dx.doi.org/10.1242/jcs.027680

Suzuki, H., K. Nishikawa, Y. Hiroaki, and Y. Fujiyoshi. 2008. Formation of aquaporin-4 arrays is inhibited by palmitoylation of N-terminal cysteine residues. *Biochim. Biophys. Acta*. 1778:1181–1189. http://dx.doi.org/10.1016/j.bbamem.2007.12.007

Tajima, M., J.M. Crane, and A.S. Verkman. 2010. Aquaporin-4 (AQP4) associations and array dynamics probed by photobleaching and single-molecule analysis of green fluorescent protein-AQP4 chimeras. *J. Biol. Chem.* 285:8163–8170. http://dx.doi.org/10.1074/jbc.M109.093948

Tham, D.K., and H. Moukhles. 2011. Regulation of Kir4.1 and AQP4 expression and stability at the basolateral domain of epithelial MDCK cells by the extracellular matrix. *Am. J. Physiol. Renal Physiol.* 301:F396–F409. http://dx.doi.org/10.1152/ajprenal.00315.2010

van de Linde, S., A. Löschberger, T. Klein, M. Heidbreder, S. Wolter, M. Heilemann, and M. Sauer. 2011. Direct stochastic optical reconstruction microscopy with standard fluorescent probes. *Nat. Protoc.* 6:991–1009. http://dx.doi.org/10.1038/nprot.2011.336

Van Hoek, A.N., R. Bouley, Y. Lu, C. Silberstein, D. Brown, M.B. Wax, and R.V. Patil. 2009. Vasopressin-induced differential stimulation of AQP4 splice variants regulates the in-membrane assembly of orthogonal arrays. *Am. J. Physiol. Renal Physiol.* 296:F1396–F1404. http://dx.doi.org/10.1152/ajprenal.00018.2009

Wilcock, D.M., M.P. Vitek, and C.A. Colton. 2009. Vascular amyloid alters astrocytic water and potassium channels in mouse models and humans with Alzheimer's disease. *Neuroscience*. 159:1055–1069. http://dx.doi.org/10.1016/j.neuroscience.2009.01.023

Yang, B., T. Ma, and A.S. Verkman. 1995. cDNA cloning, gene organization, and chromosomal localization of a human mercurial insensitive water channel. Evidence for distinct transcriptional units. *J. Biol. Chem.* 270:22907–22913. http://dx.doi.org/10.1074/jbc.270.39.22907

Yang, B., D. Brown, and A.S. Verkman. 1996. The mercurial insensitive water channel (AQP-4) forms orthogonal arrays in stably transfected Chinese hamster ovary cells. *J. Biol. Chem.* 271:4577–4580. http://dx.doi.org/10.1074/jbc.271.9.4577

Zhang, Y., Y. Bekku, Y. Dzhashiashvili, S. Armenti, X. Meng, Y. Sasaki, J. Milbrandt, and J.L. Salzer. 2012. Assembly and maintenance of nodes of ranvier rely on distinct sources of proteins and targeting mechanisms. *Neuron*. 73:92–107. http://dx.doi.org/10.1016/j.neuron.2011.10.016